Title
Role of Point Defects in Spinel Mg Chalcogenide Conductors

Journal
Chemistry of Materials, 29(22)

ISSN
0897-4756

Authors
Canepa, Pieremanuele
Gautam, Gopalakrishnan Sai
Broberg, Danny
et al.

Publication Date
2017-11-28

DOI
10.1021/acs.chemmater.7b02909

Peer reviewed

CHEMISTRY OF MATERIALS
Article
Cite This: Chem. Mater. XXXX, XXX, XXX-XXX
pubs.acs.org/cm

Role of Point Defects in Spinel Mg Chalcogenide Conductors

Pieremanuele Canepa,*[,†,∥,⊥] Gopalakrishnan Sai Gautam,[†,‡,∥] Danny Broberg,[§] Shou-Hang Bo,[†] and Gerbrand Ceder*[,†,‡,§]

[†]Materials Science Division, Lawrence Berkeley National Laboratory, Berkeley, California 94720, United States
[‡]Department of Materials Science and Engineering, Massachusetts Institute of Technology, Cambridge, Massachusetts 02139, United States
[§]Department of Materials Science and Engineering, University of California Berkeley, Berkeley, California 94720, United States

Supporting Information

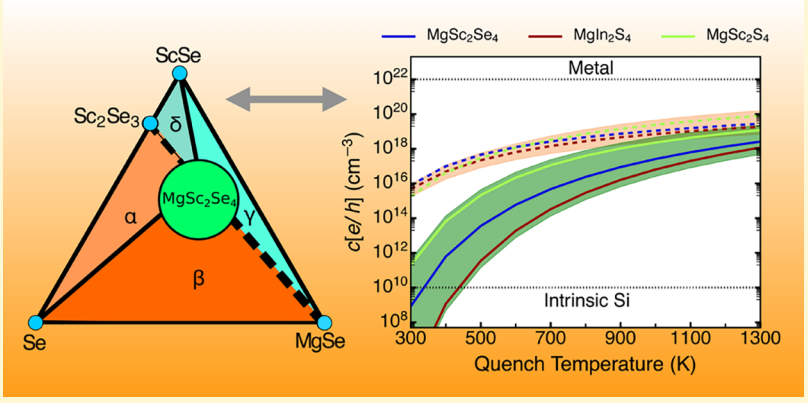

ABSTRACT: Close-packed chalcogenide spinels, such as $MgSc_2Se_4$, $MgIn_2S_4$, and $MgSc_2S_4$, show potential as solid electrolytes in Mg batteries, but are affected by non-negligible electronic conductivity, which contributes to self-discharge when used in an electrochemical storage device. Using first-principles calculations, we evaluate the energy of point defects as a function of synthesis conditions and Fermi level to identify the origins of the undesired electronic conductivity. Our results suggest that Mg-vacancies and Mg-metal antisites (where Mg is exchanged with Sc or In) are the dominant point defects that can occur in the systems under consideration. While we find anion-excess conditions and slow cooling to likely create conditions for low electronic conductivity, the spinels are likely to exhibit significant n-type conductivity under anion-poor environments, which are often present during high-temperature synthesis. Finally, we explore extrinsic aliovalent doping to potentially mitigate the electronic conductivity in these chalcogenide spinels. The computational strategy is general and can be easily extended to other solid electrolytes (and electrodes) to aid the optimization of the electronic properties of the corresponding frameworks.

1. INTRODUCTION

Chalcogenide materials, based on sulfur, selenium, and tellurium, are used in a range of technological applications, including thermoelectric materials,[1,2] semiconductors for light adsorbents and electronics,[3−11] superconductors,[12−16] Li-ion battery materials,[17−22] quantum-dots,[23−27] and more recently, topological insulators.[28,29] Specifically, sulfides have already seen applications as solid electrolytes (or superionic conductors) in solid-state Li-ion batteries.[19−21] The chalcogenide defect chemistry, either in terms of intrinsic point defects or extrinsic substitutional impurities, has often been deemed responsible for their respective figures of merit.[30,31]

Recently, ternary Mg chalcogenide spinels were also identified as possible high-mobility Mg conductors.[22] This is relevant for the possible development of Mg transport coatings or solid-state electrolytes for Mg batteries,[22] which have the potential to outperform Li-ion batteries in terms of energy density.[32] The good Mg conductivity in the $MgSc_2Se_4$, $MgIn_2S_4$, and $MgSc_2S_4$ spinels is, however, plagued by non-negligible electronic conductivity.[22] Though the significant Mg ionic conductivity $\sigma_{ionic} \sim 0.1$ mS cm^{-1} (at 298 K) is observed in $MgSc_2Se_4$ (via ^{25}Mg magic angle spin solid-state NMR and AC impedance spectroscopy), the electronic conductivity of $MgSc_2Se_4$ is ∼0.04% of the ionic conductivity,[22] and substantially larger than in other state-of-the-art alkali-(Li- and Na-)ion conductors ($\sigma_{electronic}/\sigma_{ionic}$ 10^{-4}−10^{-6}%).[19] Analogous to studies in semiconductor applications,[33] both intrinsic and extrinsic structural defects can cause large variations in electron (hole) conductivity in ionic conductors. Thus, we explore the defect chemistry of $MgSc_2Se_4$, $MgSc_2S_4$, and $MgIn_2S_4$ using first-principles calculations and aim to understand how structural defects modulate the electronic

Received: July 11, 2017
Revised: October 11, 2017
Published: October 26, 2017

DOI: 10.1021/acs.chemmater.7b02909
Chem. Mater. XXXX, XXX, XXX−XXX

properties in the bulk spinels, identify the origin of the undesired electronic conductivity, and propose practical remedies.

In detail, our calculations suggest that intrinsic point defects, such as Sc^{3+} substituting on Mg^{2+} sites in $MgSc_2S_4$ or $MgSc_2Se_4$ ($Sc_{Mg}^{\bullet}$ using the Kröger–Vink notation), and $In_{Mg}^{\bullet}$ and Mg_{In}' in $MgIn_2S_4$, can give rise to significant electronic conductivity in these materials. Additionally, our data demonstrates that anion-rich and anion-poor synthesis conditions should give rise to qualitatively different defects, affecting the electronic (hole) conductivity of these materials. Finally, we demonstrate that understanding and controlling the defect chemistry of solid electrolytes (and cathode materials) is crucial in all aspects, such as tuning the respective synthesis conditions and optimizing the electronic and ionic conductivities.

2. METHODOLOGY

2.1. Basics of Defect Chemistry. The occurrence of a defect X of charge q in a solid relates to its formation energy $E^f[X^q]$:

$$E^f[X^q] = E_{tot}[X^q] - E_{tot}[\text{bulk}] - \sum_i n_i\mu_i + qE_{Fermi} + E_{corr} \quad (1)$$

where, $E_{tot}[X^q]$ and $E_{tot}[\text{bulk}]$ are the total energies of a supercell containing the defect X and an undefected supercell, respectively.[33−37] n_i is the concentration of species i added ($n_i > 0$) or removed ($n_i < 0$) to create defect X. μ_i is the chemical potential of species i, as determined by the set of phases in thermodynamic equilibrium with the solid of interest at 0 K. E_{Fermi} is the Fermi energy of electrons in the structure, and E_{corr} is the electrostatic correction term to account for spurious interactions among defects (i.e., with periodic images and the homogeneous background charge). Using eq 1, the defect formation energies $E^f[X^q]$ can be plotted as a function of the Fermi energy, E_{Fermi}, as demonstrated in Figure 3.

In this work, we compute E_{corr} using the Freysoldt correction scheme,[33,38−40] which separates the electrostatic interactions into a short-range (decaying to zero in a large supercell) and a long-range ($\sim\frac{1}{\varepsilon r}$ beyond the supercell boundaries) component. The dielectric constants (ε's) of the spinels, utilized to approximate the long-range part of the electrostatic interactions, are reported in Table S2. For a given defect, the value of E_{corr} within the Freysoldt scheme[38,39] is determined by the convergence of the short-range potential to a constant value with increasing supercell size (as seen in Figure S1). Recently, Komsa et al.[41] determined the Freysoldt scheme to be more efficient than other schemes,[41−46] in terms of the supercell size required to achieve convergence, and quantified the average error of the Freysoldt correction to be ∼0.09 eV in a variety of systems.[41] Specifically for the MgA_2Z_4 spinels (A = Sc/In, Z = S/Se), we use a 2 × 2 × 2 supercell of the conventional cubic cell, which contains 256 anions.

Throughout the article the Kröger–Vink notation is employed to identify the type of point defects in the MgA_2Z_4 spinels, including chalcogenide vacancies (e.g., Vac_{Se}), metal vacancies (Vac_{Mg}, Vac_{Sc}), chalcogenide antisites (Se_{Mg}, Se_{Sc}), and metal antisites (Mg_{Sc}, Sc_{Mg}). For example, $Sc_{Mg}^{\bullet}$ identifies a positively charged antisite defect, where a Sc^{3+} atom replaces Mg^{2+}. Similarly, Vac_{Mg}'' and $Mg_{Sc}^{\times}$ represent a double-negatively charged vacancy on a Mg site and a neutral Mg antisite on Sc, respectively.

2.2. Charge Neutrality. Point defects can be neutral or charged species. An example is shown in Figure S2, where the donor defect is positively charged for ($q = 1$) $E_{Fermi} < \epsilon(+/0)$, while for $E_{Fermi} > \epsilon(+/0)$ the donor defect is neutral ($q = 0$). Thus, $\epsilon(+/0)$ is the thermodynamic defect transition level where two different charge states of a defect have the same E^f. The availability of electrons is set by the equilibrium Fermi level E_{Fermi}^{eq}, and the defect transition level sets the E_{Fermi}^{eq} within the band gap and, in turn, the electronic conductivity of the structure.

When multiple defects and charge states are present in a structure, estimation of E_{Fermi}^{eq} requires a self-consistent search (as explained in Figure 1) by enforcing charge neutrality of the material, corresponding

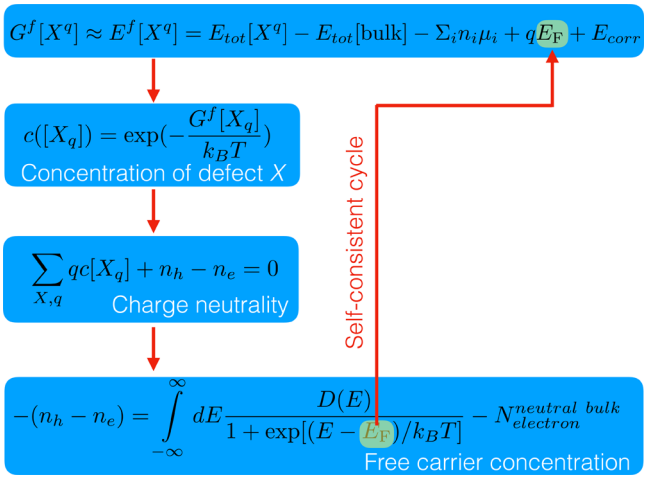

Figure 1. Self-consistent search of the equilibrium Fermi level (E_F), defect ($c[X^q]$), and free-carrier (n_h and n_e) concentrations at a given temperature (T). The chemical potentials (μ_i's) are required as input parameters.

to $\sum_{X,q} qc[X^q] + n_h - n_e = 0$. n_h (n_e) is the hole (electron) concentration, obtained by integrating the density of states [DOS, $D(E)$ in Figure 1] at a given Fermi level (E_F) in the structure. $N_{electron}^{neutral,bulk}$ in Figure 1 is the total number of electrons in the neutral bulk cell. $c[X^q]$ is the concentration of defect X^q, stemming from the Gibbs energy of defect formation, $G^f[X^q] \approx E^f[X^q]$, as $c[X^q] \approx \exp(-E^f[X^q]/k_BT)$. The resulting E_{Fermi}^{eq} and defect concentrations correspond to thermodynamic equilibrium as a function of temperature. Note that, in all the materials considered in this work (Section 4), we list a few defects as "dominant" because of their low formation energies at E_{Fermi}^{eq}.

Materials that are normally synthesized at a high temperature (∼1273 K, for example[22]), and rapidly cooled to room temperature, may have their high-temperature intrinsic defect concentrations "frozen-in" (or quenched) at room temperature, while the free-carrier concentration ($n_h - n_e$) changes with temperature, given the fixed defect concentration. A change in intrinsic defect concentration will require significant atomic diffusion, which is likely to be kinetically limited at low temperatures. Hence, for calculating defect concentrations and the Fermi level, we have considered two scenarios within the constraint of charge neutrality: (i) Defect concentrations, equilibrium Fermi level (E_{Fermi}^{eq}), and free-electron/hole concentrations ($c[e/h]^{eq}$) are self-consistently calculated at 300 K corresponding to equilibrium conditions (as in Figure 1). (ii) Defect concentrations are quenched from a higher synthesis temperature while the resulting Fermi level (E_{Fermi}^{frozen}) and free-carrier concentrations ($c[e/h]^{frozen}$) are computed at 300 K. When quenched or frozen conditions are assumed, the defect concentrations are calculated self-consistently at a higher quench temperature (i.e., 1273 K with the procedure in Figure 1), and are not allowed to change when the Fermi level and the free-carrier concentrations are recalculated at 300 K. Since defect concentrations are proportional to temperature, the frozen approximation can quantify the possible deviation from equilibrium in both defect and free-carrier concentrations at 300 K.

2.3. Computational Details. The total energies in eq 1 are obtained with density functional theory[47,48] (DFT) using the Perdew–Burke–Ernzerhof (PBE) functional within the spin-polarized generalized gradient approximation,[49] as implemented in the VASP code.[50,51] Projector augmented wave theory[52,53] and a plane-wave basis set with a cutoff of 520 eV are used to describe the crystalline wave functions, which are subsequently sampled on a dense (minimum of 1000 k-points per atom in reciprocal space) Γ-centered

DOI: 10.1021/acs.chemmater.7b02909
Chem. Mater. XXXX, XXX, XXX−XXX

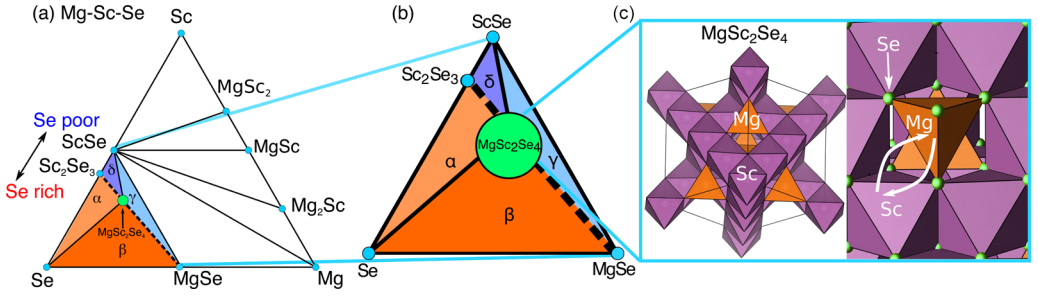

Figure 2. (a) Ternary Mg−Sc−Se phase-diagram at 0 K computed from DFT data combined with Materials Project data,[56] with (b) a zoom-in of the concentration range of interest. (c) Crystal structure of a normal spinel, such as $MgSc_2Se_4$ identified in the phase-diagrams of panels (a) and (b). The right fragment in panel (c) shows the scenario of spinel inversion (white arrows Mg ↔ Sc) in $MgSc_2Se_4$, leading to antisite Mg_{Sc} and Sc_{Mg} defects. Similar ternary phase-diagrams for $MgIn_2S_4$ and $MgSc_2S_4$ are shown in Figure S4.

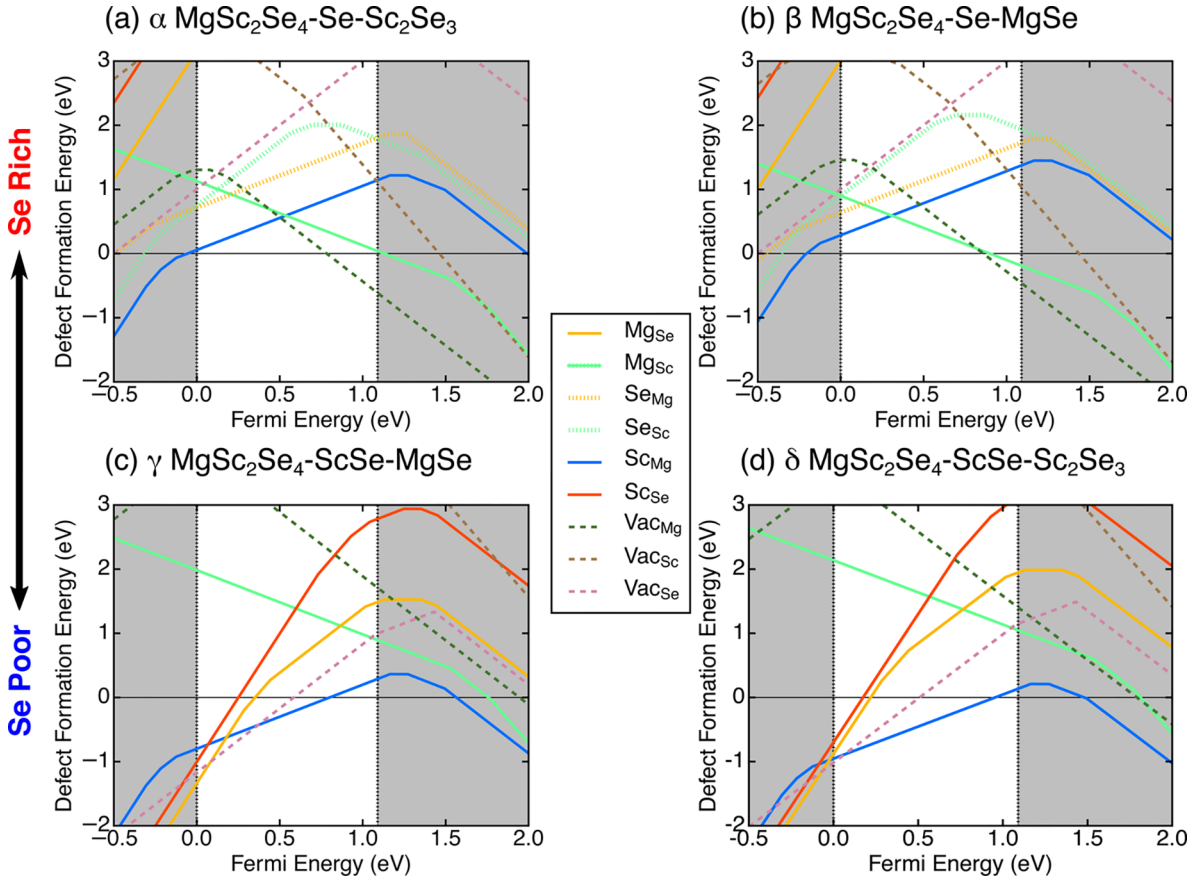

Figure 3. Defect energy $E^f[X^q]$ for intrinsic point defects (in Kröger−Vink notation) of $MgSc_2Se_4$ in four facets, (a−d) α, β, γ and δ, respectively, of the Mg−Sc−Se phase-diagram. Regions α and β are Se-rich, whereas γ and δ are Se-poor. The VBM is arbitrarily set to 0 eV, and the white region spans the band gap (~1.09 eV). Vac in the legend and dashed lines indicate vacancy defects while solid lines correspond to antisite defects.

k-point mesh.[54] The Python Materials Genomics (pymatgen)[55] and the Python Charged Defect Toolkit (PyCDT)[40] libraries are leveraged for input preparation and data analysis. For calculating the chemical potentials of the various species involved in the defect calculations, we utilize the Materials Project database[56] in addition to our own calculations.

In order to sample the large chemical space of defects, we use the computationally inexpensive semilocal PBE exchange-correlation functional, especially because the nature of the valence and conduction bands of the spinels considered, which are populated by the chalcogen (S/Se) and the metal (In/Sc) states, respectively, do not change with a higher level of theory, such as HSE06[57,58] (see Figure S3[59] in the SI). To confirm this hypothesis we performed calculations of the low-lying defects in $MgIn_2S_4$ (see Section 4.2) utilizing both GGA and HSE06, and the comparison is detailed in Section S9 of the SI.

In general, PBE is known to underestimate the band gap in most solids (by at least 30%[60]) when compared to HSE06 (Figure S3). For example, the PBE-computed direct band gaps are ~1.77, ~1.56, and ~1.09 eV for the $MgIn_2S_4$, $MgSc_2S_4$, and $MgSc_2Se_4$, respectively, while the magnitudes of the gaps increase with HSE06,[61] ~2.82 eV in $MgIn_2S_4$, ~2.63 eV in $MgSc_2S_4$, and ~2.03 eV in $MgSc_2Se_4$ (Figure S3). Note that the band gaps decrease while moving down the chalcogenide group (i.e., S → Se), under both PBE and HSE06 calculations.

3. MgA_2Z_4 STRUCTURE AND PHASE-DIAGRAM

The spinel structure MgA_2Z_4 (with A = In or Sc, and Z = S or Se), crystallizes with the anions in the face centered cubic (fcc) packing (space group, $Fd\bar{3}m$). In "normal" spinel structures, the

DOI: 10.1021/acs.chemmater.7b02909
Chem. Mater. XXXX, XXX, XXX−XXX

higher-valent cations (A = In^{3+} or Sc^{3+}), occupy octahedral (oct) sites 16*d*, as shown by the purple polyhedra in Figure 2c, and the Mg^{2+} occupy the tetrahedral (tet) 8*a* sites (orange polyhedra). Few spinels, such as $MgIn_2S_4$, can also exhibit "inversion", as experimentally observed by Gastaldi et al.,[62] where a fraction of Mg^{2+} ions in the 8*a* exchange sites with the In^{3+} in 16*d*.

The ternary 0 K phase-diagrams of Figure 2a,b depict four phases: Se, MgSe, ScSe, and Sc_2Se_3 that can be in thermodynamic equilibrium with the ternary $MgSc_2Se_4$ spinel, at different atomic chemical potentials (μ_{Se} and μ_{Mg}). Equivalent phase-diagrams have been constructed for the Mg−In−S and Mg−Sc−S systems and are presented in Figure S4a,b of the SI. The four different facets of Figure 2a,b, namely, α $MgSc_2Se_4$−Se−Sc_2Se_3 (light orange), β $MgSc_2Se_4$−Se−MgSe (dark orange), γ $MgSc_2Se_4$−MgSe−ScSe (dark violet), and δ $MgSc_2Se_4$−ScSe−Sc_2Se_3 (light violet), define the possible limiting chemical potential values (μ_i of eq 1) for intrinsic point defect formation, such as vacancies (e.g., Vac_{Mg}) and antisites (e.g., Mg_{Sc}).

Subsequently, the α- and β-facets can be classified as "Se-rich" domains, owing to elemental Se forming one of the bounding vertices of the respective facets, while γ and δ are "Se-poor". The dashed line in Figure 2a,b highlights the binary precursors, MgSe and Sc_2Se_3, which are used for the high-temperature synthesis (~1200 °C) of $MgSc_2Se_4$.[12] Off-stoichiometry of $MgSc_2Se_4$ will place the thermodynamic equilibrium during synthesis into one of the four facets (α–δ), which in turn can influence the $E^f[X^q]$ and the defect concentrations.

4. NATIVE DEFECTS

4.1. $MgSc_2Se_4$. Figure 3 shows the formation energies $E^f[X^q]$ of intrinsic defects in $MgSc_2Se_4$ obtained for the chemical potential in each of the four facets in the Mg−Sc−Se system, namely, $MgSc_2Se_4$−Se−Sc_2Se_3 α (Figure 3a), $MgSc_2Se_4$−Se−MgSe β (Figure 3b), $MgSc_2Se_4$−MgSe−ScSe γ (Figure 3c), and $MgSc_2Se_4$−MgSe−Sc_2Se_3 δ (Figure 3d). The *y*-axis of each panel in Figure 3 plots the defect energy against the E_{Fermi} (*x*-axis) in $MgSc_2Se_4$. The absolute value of the Fermi energy is referenced to the valence band maximum (VBM) energy of the pristine $MgSc_2Se_4$ bulk. The zero of the *x*-axis is the VBM, with gray shaded regions being the valence (E_{Fermi} < 0) and the conduction (E_{Fermi} > E_{gap} ~ 1.09 eV) bands, respectively. The band gap spans the white area in all panels of Figure 3. In general, the defect levels with low formation energies in the band gap can considerably alter the intrinsic electronic conductivity of semiconductors and insulators, thus forming the region of interest in this analysis.

Facets α and β (Figure 3a,b) are Se-rich, and show qualitatively similar defect energetics. For example, the defects with the lowest $E^f[X^q]$ are the Sc_{Mg}, Mg_{Sc}, and Vac_{Mg} in both α and β. Sc_2Se_3 has been previously detected as a prominent impurity in the synthesis of $MgSc_2Se_4$,[22] thus motivating the choice of facet α ($MgSc_2Se_4$−Se−Sc_2Se_3) to characterize the Se-rich domain. Similar conclusions are deduced by comparing the γ- and δ-facets (Figure 3c,d), with comparable $E^f[X^q]$ for the low-lying defects (e.g., Sc_{Mg}), and only the γ phase is considered further to analyze the Se-poor domain. Analogous behaviors are also observed for $MgSc_2S_4$ and $MgIn_2S_4$, showing similar trends for the S-rich and S-poor domains (Figures S5 and S6 in the SI).

Se-rich Domain, α $MgSc_2Se_4$−Se−Sc_2Se_3. The dominant defects within the band gap of the Se-rich region are the charged $Sc_{Mg}^{\bullet}$, Mg_{Sc}', and Vac_{Mg}'' (dark blue, light green, and dashed green lines, respectively, in Figure 3a). A charged defect always exchanges its excess (deficient) charge with the electron reservoir of the structure, whose energy is given by the Fermi energy. Thus, the n-type $Sc_{Mg}^{\bullet}$ exchanges the excess valence electron from Sc with the Fermi level of $MgSc_2Se_4$. Analogous considerations extend to the p-type Mg_{Sc}', where one electron is added to the antisite from the Fermi level.

Given that the opposite charges of $Sc_{Mg}^{\bullet}$, Mg_{Sc}', and Vac_{Mg}'' can potentially charge-compensate each other leading to charge neutrality, the E_{Fermi}^{eq} is nominally pinned at a Fermi energy where all three defects have similar E^f. Indeed, a self-consistent calculation of the E_{Fermi}^{eq} at 300 K (i.e., assuming defect concentrations equilibrate at 300 K) leads to E_{Fermi} = 0.46 eV (see Figure 3a, and Figure S5a in the SI), with defect concentrations of 7.9 × 10^{11} cm^{-3} for $Sc_{Mg}^{\bullet}$, 2.4 × 10^{11} cm^{-3} for Mg_{Sc}', and 2.8 × 10^{11} cm^{-3} for Vac_{Mg}''. Typically, defect contents above 10^{15} cm^{-3} are detectable via experiments, such as electron paramagnetic resonance.[33,63,64] Alternatively, defect concentrations can be expressed in units per atom or per formula unit. For example, a defect concentration of 10^{15} cm^{-3} in $MgSc_2Se_4$ corresponds to ~2.4 × 10^{-8} $atom^{-1}$ and 1.7 × 10^{-7} $(formula\ unit)^{-1}$, respectively. For the α-facet of $MgSc_2Se_4$ at 300 K, the Fermi level is "deep" within the band gap, which will lead to low electronic (or hole) conductivity since large thermal energies ($\gg k_BT$) will be required to ionize free electrons (holes) from the E_{Fermi}^{eq} into the conduction (valence) band. Qualitatively similar conclusions can be drawn from the analysis of the defects in the β-facet (Figure 3b and Figure S7a).

However, when defect concentrations are frozen-in from a higher temperature (~1273 K used for $MgSc_2Se_4$ synthesis[22]), the E_{Fermi}^{frozen} at 300 K drops below the VBM (~−0.10 eV) indicating that the material becomes a p-type conductor. Thus, significant hole conductivity can be expected under frozen defect conditions, with free hole concentration of ~2.6 × 10^{18} cm^{-3} (~0.0001 per lattice site), which is beyond undoped semiconductor levels (~10^{10} cm^{-3} in the SI), but below metallic levels (~1 charge carrier per lattice site). As the temperature at which the defect concentrations are quenched decreases, the E_{Fermi}^{frozen} recovers beyond the VBM and reaches ~0.02 eV at 800 K (Figure S7a), indicating the importance of slow cooling conditions to reduce hole conductivity during the synthesis of $MgSc_2Se_4$.

Se-Poor Domain, γ $MgSc_2Se_4$−ScSe−MgSe. The Se-poor region (Figure 3c) is dominated by n-type defects, such as $Sc_{Mg}^{\bullet}$ (dark blue), $Vac_{Se}^{\bullet\bullet}$ (dashed red), and $Mg_{Se}^{\bullet\bullet\bullet}$ (orange). Although the formation energies of a few defects are negative across the band gap, as in the case of $Sc_{Mg}^{\bullet}$ for E_{Fermi} < 0.7 eV (Figure 3c), the spontaneous formation of such charged defects is constrained by the condition of charge neutrality in $MgSc_2Se_4$.

The self-consistent equilibrium Fermi level (~1.08 eV at 300 K) for the Se-poor region is mainly set by the $Sc_{Mg}^{\bullet}$ defect. However, for temperatures above 300 K, the E_{Fermi}^{eq} exceeds the conduction band minimum (CBM, ~1.1 eV, Figure S7a), suggesting the occurrence of spontaneous electronic conductivity when the spinel is synthesized under Se-poor conditions. Furthermore, when defect concentrations are frozen-in from ~1273 K, E_{Fermi}^{frozen} is well above the CBM (~1.4 eV) at 300 K, suggesting that fast cooling during synthesis will likely increase the electronic conductivity. Similar conclusions can be extended by evaluating the defect energies in the δ-facet

DOI: 10.1021/acs.chemmater.7b02909
Chem. Mater. XXXX, XXX, XXX−XXX

(Figure 3d, and Figure S7a in the SI), where the equilibrium Fermi level is beyond the CBM even at 300 K, suggesting that preventing intrinsic electronic conductivity in $MgSc_2Se_4$ in Se-poor conditions may be challenging.

4.2. $MgIn_2S_4$. Figure 4 plots the defect formation energies for the S-rich (α) and S-poor (γ) domains as a function of

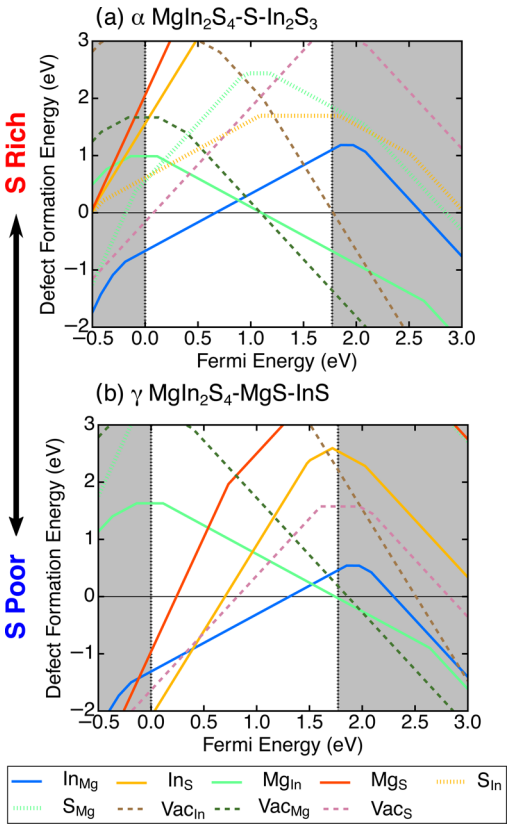

Figure 4. $E^f[X^q]$ for intrinsic point defects (in Kröger–Vink notation) of $MgIn_2S_4$ for (a, b) two regions of the phase-diagram (α and γ, respectively; refer to Figure 3). Region α is S-rich, whereas γ is S-poor. The VBM is set to 0 eV, and the white region is the band gap (~1.77 eV). Vac in legend and dashed lines indicate vacancy defects while solid lines correspond to antisite defects.

Fermi energy in the $MgIn_2S_4$ spinel. Analogous to $MgSc_2Se_4$ (Figure 3a), the stable defects in the S-rich domain of $MgIn_2S_4$ (Figure 4a) include the n-type $In^{\bullet}_{Mg}$ (solid blue), and the p-type Mg'_{In} (light green) and Vac''_{Mg} (dashed green). For the α-facet (S-rich domain), the resulting E^{eq}_{Fermi} is ~0.88 eV at 300 K, corresponding to a free hole concentration of $\sim 6.46 \times 10^4$ cm^{-3}. Other notable defects, such as Vac'''_{In}, $Vac^{\bullet\bullet}_{S}$, and S'_{In}, are not expected to play a dominant role in $MgIn_2S_4$.

Since the equilibrium Fermi energy is pinned near the middle of the band gap (~0.88 eV Figure 4a) by self-compensating charged defects, the material will exhibit low electronic conductivity under equilibrium S-rich conditions. Nevertheless, the equilibrium defect concentrations are significant, $\sim 4.9 \times 10^{17}$ cm^{-3} for $In^{\bullet}_{Mg}$, 4.9×10^{17} cm^{-3} for Mg'_{In}, and 7.8×10^{13} cm^{-3} for Vac''_{Mg}. Such high concentrations of antisite $In^{\bullet}_{Mg}$ and Mg'_{In} defects indicate that the spinel undergoes a high degree of "inversion", Mg and In exchanging their lattice sites,[65] besides exhibiting significant Mg-vacancies during S-rich synthesis conditions.

The analysis of the defect formation energies in the S-poor-facet (γ, Figure 4b) suggests that the $Vac^{\bullet}_{S}$ and $In^{\bullet\bullet}_{S}$ defects can influence E^{eq}_{Fermi}, apart from the $In^{\bullet}_{Mg}$, Mg'_{In}, and Vac''_{Mg}. Interestingly, the self-consistent Fermi level of the γ-facet is ~1.53 eV, which corresponds approximately to charge-compensation between the $In^{\bullet}_{Mg}$ and Mg'_{In} defects. Furthermore, the equilibrium defect concentrations ($\sim 4.9 \times 10^{17}$ for both $In^{\bullet}_{Mg}$ and Mg'_{In}, separately) estimated under S-poor conditions compare well with a S-rich environment, indicating that the $MgIn_2S_4$ is expected to undergo a substantial degree of spinel inversion irrespective of synthesis conditions, in agreement with experimental observations.[65]

Similar to $MgSc_2Se_4$, cooling rates during synthesis are expected to play a major role in determining the intrinsic hole/electronic conductivity in the In spinel (Figure S7b). For example, under frozen-in defect concentrations from ~1273 K, the E^{frozen}_{Fermi} and $c[e/h]^{frozen}$ are ~0.10 eV, 1.17×10^{18} (free holes) for S-rich; and ~1.80 eV (>CBM), 1.12×10^{19} (free electrons) for S-poor, respectively. $MgIn_2S_4$ is expected to exhibit p-type and n-type conductivity in S-rich and S-poor conditions, respectively, under quenched defect concentrations. Thus, the protocols to synthesize $MgIn_2S_4$ require careful tuning to allow for slow cooling and S-rich conditions.

4.3. $MgSc_2S_4$. Figure 5 shows the formation energies of native defects of $MgSc_2S_4$ in both S-rich (α-facet) and S-poor (γ-facet) domains. The defect energetics in $MgSc_2S_4$ are similar to those in the Se spinel, in the anion-rich domain (Figure 5a), with the dominant defects being $Sc^{\bullet}_{Mg}$, Mg'_{Sc}, and Vac''_{Mg}. The E^{eq}_{Fermi}, calculated self-consistently at 300 K, is ~0.4 eV and

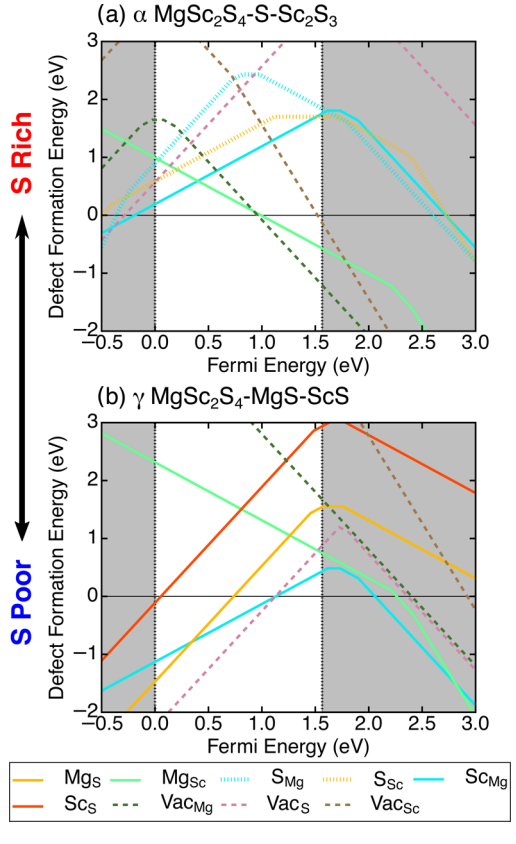

Figure 5. $E^f[X^q]$ for intrinsic point defects (in Kröger–Vink notation) of $MgSc_2S_4$ for (a, b) two regions of the phase-diagram (α and γ, respectively; refer to Figure 3). Region α is S-rich, whereas γ is S-poor. The VBM is set to 0 eV, and the white region is the band gap (~1.56 eV). Vac in legend and dashed lines indicate vacancy defects, and solid lines indicate antisite defects.

DOI: 10.1021/acs.chemmater.7b02909
Chem. Mater. XXXX, XXX, XXX–XXX

roughly corresponds to the self-compensation of Vac''_{Mg} and Mg'_{Sc} with $Sc^{\bullet}_{Mg}$. Therefore, when $MgSc_2S_4$ is prepared under S-rich conditions, it should exhibit a small degree of spinel inversion ($Sc^{\bullet}_{Mg}$ 1.7×10^{11} cm^{-3}, and $Mg'_{Sc} \sim 3.7 \times 10^{11}$ cm^{-3}), and low hole conductivity ($c[h]^{eq} \sim 2.01 \times 10^{11}$ cm^{-3}). Also, under frozen-in defect conditions (from 1273 K), $MgSc_2S_4$ becomes a spontaneous p-type conductor similar to $MgSc_2Se_4$, with E_{Fermi}^{frozen} drifting below the VBM (~−0.06 eV) resulting in a larger $c[h]^{frozen} \sim 1.18 \times 10^{19}$ cm^{-3}.

The dominant point defects in the S-poor region (γ, Figure 5b) are $Mg^{\bullet\bullet}_S$, $Sc^{\bullet}_{Mg}$, $Vac^{\bullet\bullet}_S$, and Mg'_{Sc}, with $Vac^{\bullet\bullet}_S$ displaying the lowest $E^f[X^q]$ across the band gap, up to $E_{Fermi} \sim 1.5$ eV. In the γ-facet (and δ-facet, Figure S7c), the equilibrium Fermi level at 300 K is beyond the CBM and remains so even at 100 K, indicating spontaneous electronic conductivity under S-poor conditions. Under quenched defect conditions (from 1273 K), E_{Fermi}^{frozen} is found to be deeper into the conduction band (~1.80 eV) compared to equilibrium at 300 K (Figure S7c). Indeed, $c[e]^{eq}$ is estimated to be ~1.8×10^{15} cm^{-3} under equilibrium at 300 K, while the concentration increases by nearly 5 orders of magnitude ($c[e]^{frozen} \sim 7.8 \times 10^{19}$ cm^{-3}) under quenched conditions. Thus, suppressing intrinsic electronic conductivity in $MgSc_2S_4$ under S-poor conditions represents a major challenge.

5. EXTRINSIC DEFECTS IN $MgSc_2Se_4$

High ionic conductivity in materials is often achieved if the concentration of mobile vacancies is increased. One strategy commonly adopted to increase ionic conductivity in solid electrolytes is extrinsic doping, specifically doping the anion sublattice.[66−68] Nominally, the selection of an extrinsic dopant follows the rule of thumb of finding similar-sized cations (anions) for aliovalent substitution in the lattice. In addition, it is desirable that the substituting element is not redox-active, which will minimize the occurrence of redox side-reactions in ionic conductors.

In the case of the spinel Mg conductors discussed in this work, the electronic conductivity primarily arises from antisite defects, such as $Sc^{\bullet}_{Mg}$ and $In^{\bullet}_{Mg}$, pushing the equilibrium Fermi level close to (or beyond) the CBM level at 300 K. A pathway to curb the formation of antisite defects is doping the metal site (Sc or In) with cations that are less likely to promote spinel inversion. For example, metal ions with higher oxidations states (such as Zr^{4+} and Nb^{5+}), or those manifesting a stronger octahedral site preference than Mg^{2+}, are less likely to occupy the tetrahedral spinel sites.[69] Thus, cation doping on the Sc site can inhibit the formation of antisite Sc_{Mg} defects in $MgSc_2Se_4$ (and $MgSc_2S_4$).

Figure 6 plots the defect formation energies for extrinsic doping of several nonredox tetravalent (Ce, Ge, Sn, Pb, Ti, and Zr; solid lines in Figure 6a), and pentavalent (As, Bi, Na, and Ta; dashed lines) cations on Sc in $MgSc_2Se_4$, as well as anion doping on Se^{2-} with monovalent anions (Cl^-, Br^-, and I^-; Figure 6b). Because of the Se-poor synthesis conditions normally encountered, we restrict the analysis only to the γ-facet ($MgSc_2Se_4$−MgSe−ScSe), while calculations of the α-, β-, and δ-facets of $MgSc_2Se_4$ are discussed in Figures S7 and S8 of the SI. Note that the chemical potential of each extrinsic dopant in eq 1 is set by the most stable phase in the Mg−Sc−Se−[extrinsic dopant] phase-diagram that is in equilibrium with $MgSc_2Se_4$, MgSe, and ScSe (accessed via the Materials Project[56]). For example, in the case of Cl^- doping on Se^{2-}, μ_{Cl} is determined by the facet $MgSc_2Se_4$−MgSe−ScSe−$MgCl_2$.

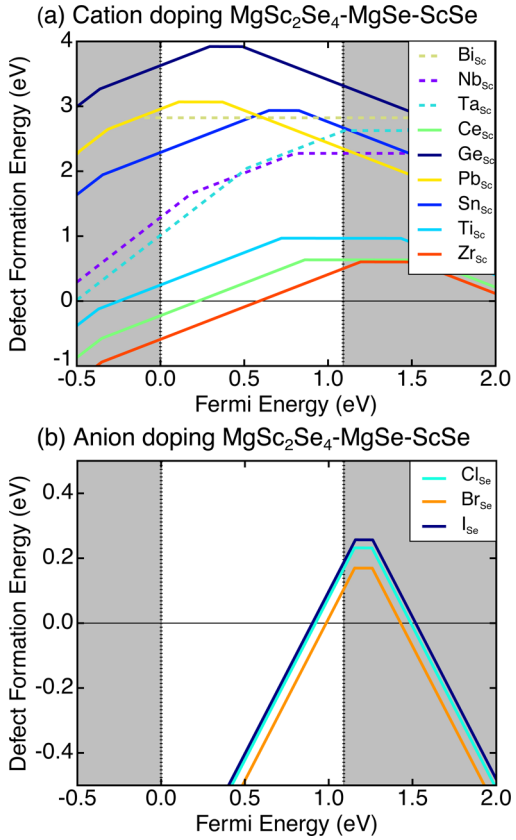

Figure 6. $E^f[X^q]$ for extrinsic (a) cation and (b) anion substitution in $MgSc_2Se_4$ under Se-poor conditions (γ-facet). In panel a, tetravalent and pentavalent cations are shown by solid and dashed lines, respectively. The VBM is set to 0 eV, and the white region is the band gap (~1.09 eV). $E^f[X^q]$ is not shown for As_{Sc} substitution, since the values are above 4 eV through the Fermi energy range considered.

Data in Figure 6 suggests that extrinsic doping of several cations, such as Bi, Nb, Ta, Ge, Sn, and Pb, on Sc in $MgSc_2Se_4$ is highly unfavorable (with $E^f[X^q] \geq 1$ eV). In contrast, halogen doping on Se (Figure 6b), Ce (solid green line in Figure 6a), Ti (solid light blue), and Zr (solid red line) doping on Sc, appear favorable. Specifically, halogen substitutions on Se and $Zr^{\bullet}_{Sc}$ show a negative formation energy over a wide portion of the band gap.

Since the behavior of halogen doping (and $Zr^{\bullet}_{Sc}$) is similar to intrinsic n-type $Sc^{\bullet}_{Mg}$ (Figure 3c) antisites, anion (and Zr) doping in $MgSc_2Se_4$ may not be beneficial since the E_{Fermi}^{eq} is likely to be pushed into the conduction band at 300 K. However, n-type $Ce^{\bullet}_{Sc}$ and $Ti^{\bullet}_{Sc}$ show fairly deep donor transition levels away from the CBM (Figure 6a). Indeed, E_{Fermi}^{eq} values at 300 K for the $Ce^{\bullet}_{Sc}$ and $Ti^{\bullet}_{Sc}$, without considering the presence of intrinsic antisites, are ~0.82 and 0.58 eV, respectively. Thus, Ce and Ti doping should not increase the electronic conductivity of $MgSc_2Se_4$, though their effect on the Sc_{Mg} formation energies requires more investigation.

6. DISCUSSION

Using first-principles defect energy calculations, we analyzed the defect chemistry in chalcogenide Mg spinels, namely, $MgSc_2Se_4$, $MgSc_2S_4$, and $MgIn_2S_4$, and have summarized the Fermi energies and free-carrier concentrations in Table 1 (defect concentrations are also tabulated in Table S1) for a representative anion-rich and anion-poor equilibrium. Under all

DOI: 10.1021/acs.chemmater.7b02909
Chem. Mater. XXXX, XXX, XXX−XXX

Table 1. Defect Energetics[a] in the MgA_2Z_4 Spinels (A = Sc, In; Z = S, Se), for Both Anion-Rich (α) and Anion-Poor (γ) Conditions (Facets)

condition	dominant defects	carrier	E_{Fermi}^{eq}	$c[e/h]^{eq}$	E_{Fermi}^{frozen}	$c[e/h]^{frozen}$
			$MgSc_2Se_4$ (E_{gap} = 1.09 eV)			
Se-rich (α)	$Sc_{Mg}^{\bullet}$, Mg_{Sc}',Vac_{Mg}''	h^+	0.46	8.42×10^8	−0.10	2.58×10^{18}
Se-poor (γ)	$Sc_{Mg}^{\bullet}$	e^-	1.08	7.96×10^{15}	1.39	2.77×10^{19}
			$MgIn_2S_4$ (E_{gap} = 1.77 eV)			
S-rich (α)	$In_{Mg}^{\bullet}$, Mg_{In}', Vac_{Mg}''	h^+	0.88	6.46×10^4	0.10	1.17×10^{18}
S-poor (γ)	$In_{Mg}^{\bullet}$, Mg_{In}', Vac_{Mg}''	e^-	1.53	4.10×10^{14}	1.80	1.12×10^{19}
			$MgSc_2S_4$ (E_{gap} = 1.55 eV)			
S-rich (α)	$Sc_{Mg}^{\bullet}$, Mg_{Sc}', Vac_{Mg}''	h^+	0.40	2.01×10^{11}	−0.06	1.18×10^{19}
S-poor (γ)	$Sc_{Mg}^{\bullet}$, Mg_{Sc}', $Vac_S^{\bullet\bullet}$	e^-	1.48	1.81×10^{15}	1.80	7.86×10^{19}

[a]Self-consistent E_{Fermi}^{eq} at 300 K (in eV) and Fermi levels with quenched defect content (from 1273 K, E_{Fermi}^{frozen}), are indicated. $c[e/h]^{eq}$ and $c[e/h]^{frozen}$ (in cm^{-3} at 300 K) are the free charge-carrier concentrations in the self-consistent equilibrium and frozen defect scenarios, with e and h for electrons and holes. The charge of the dominant defect is indicated with respect to the charged state of the defect at E_{Fermi}^{eq}.

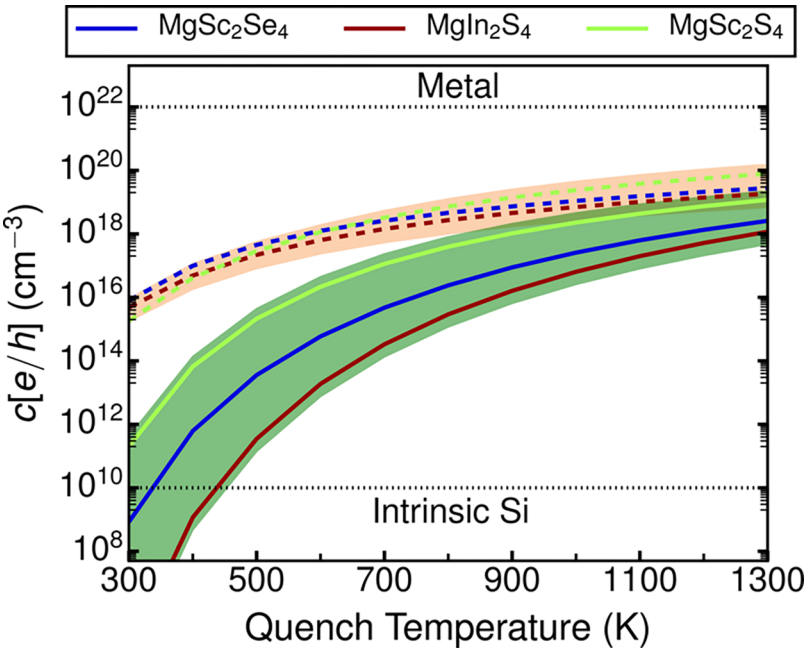

Figure 7. Free-electron or hole concentrations $c[e/h]$ at 300 K as a function of temperature at which defect concentrations are quenched. Solid and dashed lines indicate anion-rich (green-shaded) and anion-poor (orange-shaded) regions, respectively. The blue, red, and green line colors correspond to $MgSc_2Se_4$, $MgIn_2S_4$, and $MgSc_2S_4$, respectively. The dotted black lines indicate the typical free-carrier concentration in intrinsic Si (10^{10} cm^{-3}) and in metals (10^{22} cm^{-3}). The y-axis values at 300 K are the $c[e/h]^{eq}$ for each spinel, and values at 1300 K should indicate $c[e/h]^{frozen}$ corresponding to quenched defect concentrations from typical synthesis temperatures.[22] For the case of anion-rich $MgIn_2S_4$, the free-carrier concentration is taken as the maximum of free-electron and hole concentrations at each quench temperature.

conditions, antisites ($Mg_{\{Sc/In\}}$ and $\{Sc/In\}_{Mg}$) and Mg-vacancies are the dominant defects, while anion-vacancies only appear for $MgSc_2S_4$ under S-poor conditions.

6.1. Anion-Rich vs Anion-Poor Conditions. All three spinels display markedly different defect energetics in the anion-rich (S-/Se-rich) and anion-poor domains, under equilibrium defect concentrations. In the case of anion-rich conditions (α-facet), the spinels exhibit marginal p-type behavior with low carrier concentrations, due to the presence of charged antisites ($\{Sc/In\}_{Mg}^{\bullet}$ and $Mg_{\{Sc/In\}}'$), and Vac_{Mg}'', which charge-compensate each other and pin the E_{Fermi}^{eq} within the respective band gaps. Since the E_{Fermi}^{eq} is far away from the VBM (or CBM), i.e., $\gg k_BT$, the hole (or electronic) conductivity is not expected to be significant (see Table 1). Hence, the synthesis of the chalcogenide conductors in anion-rich environments should curtail, to a large extent, the undesired hole/electron conductivity for application as a Mg solid electrolyte. However, synthesis of the Se spinels requires high temperatures (>1000 °C),[12,13,22] at which elemental Se (bp ∼685 °C) and S (∼444 °C) vaporize and may lead to anion-poor conditions. One potential strategy to mitigate anion loss during synthesis is to use the respective stoichiometric binaries, such as MgSe and Sc_2Se_3 to form $MgSc_2Se_4$, at high temperature.[12,13]

Unlike anion-rich conditions, the dominant n-type $Sc_{Mg}^{\bullet}$ antisites in the anion-poor domain (γ-facet) push the E_{Fermi}^{eq} beyond the CBM in both Sc spinels, ensuring spontaneous electronic conductivity. We speculate that the low $Sc_{Mg}^{\bullet}$ equilibrium concentration (∼7.96×10^{15} cm^{-3}, Table S1) in $MgSc_2Se_4$ may not significantly affect the XRD pattern[22] with respect to an ideal spinel structure and might be hard to detect using bulk characterization experiments. Also, the $c[e]^{eq} \sim 7.96 \times 10^{15}$ in $MgSc_2Se_4$ (Table 1), corresponding to ∼0.0001 free electrons per lattice site, is remarkably high compared to the

DOI: 10.1021/acs.chemmater.7b02909
Chem. Mater. XXXX, XXX, XXX−XXX

intrinsic carrier concentration of typical semiconductors (e.g., $\sim 10^{10}$ cm^{-3} in Si), but significantly below metallic levels ($\sim$1e$^-$ per lattice site). Although the $In^{\bullet}_{Mg}$ and Mg'_{In} defects charge-compensate in $MgIn_2S_4$, the E^{eq}_{Fermi} under S-poor conditions is only ~0.2 eV below the CBM, indicating significant n-type conductivity. Indeed, a previous measurement of the Hall effect in $MgIn_2S_4$[65] reported a moderate resistivity of $\sim 8.2 \times 10^3$ Ω cm^{-1} and a free-electron concentration of $\sim 6.4 \times 10^{15}$ cm^{-3}, in reasonable agreement with our $c[e]^{eq}$ estimate of $\sim 4.1 \times 10^{14}$ cm^{-3} in the γ-facet.

6.2. Impact of Cooling Rates. The variation of $c[e/h]^{frozen}$ and E^{frozen}_{Fermi} as a function of quench temperature, the temperature at which the defect concentrations are frozen, is plotted in Figure 7 and Figure S7, respectively. Solid and dashed lines in Figure 7 correspond to anion-rich and anion-poor conditions, while the blue, red, and green colors indicate $MgSc_2Se_4$, $MgIn_2S_4$, and $MgSc_2S_4$, respectively. The quench temperature, which is determined by the cooling rate, significantly impacts the hole/electron conductivity. For example, all three spinels are expected to show spontaneous hole conductivity at 300 K in the anion-rich domain (α-facet) when defect concentrations are quenched from 1300 K, contrary to the equilibrium scenario which would give negligible p-type conduction, as indicated by Figure 7 and Table 1. Furthermore, quenched defect conditions in the anion-poor domain (γ-facet) dramatically increase the n-type conductivity in all spinels, resulting in $c[e]^{frozen}$ values that are ≈3−4 orders of magnitude higher than $c[e]^{eq}$ (Table 1, Figure 7). As a result, the synthesis of the chalcogenide spinels discussed in this work requires not only anion-rich conditions but also slow cooling postsynthesis (i.e., low quench temperatures, ~400−500 K; see Figure S7) to minimize the electronic conductivity.

6.3. Inversion in $MgIn_2S_4$. In comparison to the Sc compounds, the defect energies in $MgIn_2S_4$ (Figure 4a,b) dictate that, under equilibrium, the E^{eq}_{Fermi} should be largely set by charge-compensating $In^{\bullet}_{Mg}$, Mg'_{In}, and Vac''_{Mg}, corresponding to a lower hole/electron conductivity in either S-rich or S-poor conditions. Notably, the combination of $In^{\bullet}_{Mg}$ and Mg'_{In} antisites leads to inversion in the spinel (i.e., Mg and In exchange their respective sites), resulting in a $[Mg_{1-i}In_i][Mg_iIn_{2-i}]S_4$ stoichiometry, where i is the degree of inversion.

Our calculations indicate that $MgIn_2S_4$ will display significant spinel inversion under both S-rich and S-poor equilibrium conditions, with expected concentrations of 4.9×10^{17} for both $In^{\bullet}_{Mg}$ and Mg'_{In} (Table S1), which qualitatively agrees with experimental reports.[65,70−74] Spinel inversion can impact Mg-mobility and in turn the overall ionic conductivity since inverted structures will possess multiple local Mg−In configurations.

Interestingly, the Sc-containing spinels are not expected to invert as much as the $MgIn_2S_4$. For example, $MgSc_2S_4$ exhibits fewer antisites ($Sc^{\bullet}_{Mg}$, Mg'_{Sc} ~ 10^{11} cm^{-3}) than $MgIn_2S_4$ under S-rich equilibrium conditions (Table S1). The tendency of $MgIn_2S_4$ to invert readily may be due to the sp^3 hybridization in the tetrahedra that is better accommodated by In than by Sc.

6.4. Chemical Driving Forces for Antisite Defect Formation. In the previous sections and Table 1, we have demonstrated that the dominant defects in the chalcogenide spinels are antisites, signifying that p-type Mg'_{In} and n-type $In^{\bullet}_{Mg}$ are the primary intrinsic defects in $MgIn_2S_4$, while $Sc^{\bullet}_{Mg}$ or Mg'_{Sc} are the main defects in $MgSc_2S_4(Se_4)$. These findings are similar to previous computational[75−78] and experimental[72] studies on ternary oxide spinels, with antisites dominating over other intrinsic defects, i.e., vacancies and interstitials. Given that the p-type (n-type) antisite can compensate the excess electron (hole) ionized from the oppositely charged n-type (p-type) antisite, the resulting Fermi level and the concentration of free electrons (or holes) at equilibrium depend on the difference in concentration between the p- and n-type antisites. For example, our data shows that under S-rich conditions an equal concentration of p- and n-type defects (as indicated by E^{eq}_{Fermi} and $c[e/h]^{eq}$ in $MgIn_2S_4$, Table 1 and Table S1) will pin the Fermi level within the band gap corresponding to a low concentration of free carriers.

So far, our calculations suggest that antisite concentrations (and the corresponding difference between the concentration of p- and n-type antisites) can be markedly different for the spinels considered in this work. Particularly, the results presented in Table 1 demonstrate that the concentration of antisites in $MgIn_2S_4$ is always greater by several orders of magnitude (across all chemical conditions, see Table S1) than in $MgSc_2S_4(Se_4)$. Additionally, our calculations indicate that the difference between the p- and n-type antisite concentrations in $MgIn_2S_4$ is consistently lower than the Sc spinels (Table S1), with profound effects on the type and magnitude of the electrical conductivity in the corresponding systems. Here, we rationalize the chemical factors driving such differences.

In general, the occurrence of antisites depends on a combination of several factors, such as (i) *steric effects* (i.e., the strain due to differences in ionic radii of the cations forming antisites), (ii) the *band gap* of each material (ease of ionizing the excess electron/hole), and (iii) the electronic nature or *bond character* of specific bonds (covalent or ionic).

Steric Effects. Antisites are facilitated if the cations substituting for each other possess similar ionic size. For example, Mg^{2+} has an ionic radius of ~0.57 and ~0.72 Å in tetrahedral and octahedral coordination, respectively, which compares well with the ionic radius of In^{3+} ~ 0.62 Å in tetrahedral and ~0.80 Å in octahedral coordination, respectively,[79] implying the facile formation of both Mg'_{In} and $In^{\bullet}_{Mg}$ antisites. While Sc^{3+} has an ionic radius of ~0.75 Å in octahedral sites,[79] it has never been observed in tetrahedral coordination to our knowledge.

Band Gap. Large band gaps in materials limit the possibility of ionization of the excess charge in defects, penalizing the injection of a free hole (electron) into the valence (conduction) band. Thus, the "large" band gap in $MgIn_2S_4$ (Figure S3 in the SI) indicates a high energy penalty to ionize the excess charge, forcing Mg'_{In} to charge-compensate $In^{\bullet}_{Mg}$ (and vice versa) and leading to a lower difference in concentration between Mg'_{In} and $In^{\bullet}_{Mg}$ across all conditions (Table S1). In contrast, the band gaps in Sc spinels are quantitatively lower than those in the In spinel, indicating that the energy penalty for either $Sc^{\bullet}_{Mg}$ or Mg'_{Sc} to ionize the excess charge is significantly smaller, suggesting that the Mg'_{Sc} may not be required to charge-compensate the $Sc^{\bullet}_{Mg}$. Since inversion in the spinel structure correlates with the formation of comparable quantities of both p- and n-type antisites, $MgIn_2S_4$ is more susceptible in exhibiting spinel inversion than the Sc compounds, in agreement with previous experimental studies.[65]

Bond Character. Covalent bonds with significant hybridization of the transition metal and the anion can tolerate antisites better than ionic bonds, because of greater electrostatic screening of the excess charge in the antisites. Since each octahedral (16*d*) site in the spinel structure shares edges with 6

DOI: 10.1021/acs.chemmater.7b02909
Chem. Mater. XXXX, XXX, XXX−XXX

other 16*d* sites (Figure 2),[80] electrostatic screening will be important in stabilizing the p-type antisites (i.e., Mg'_{In} and Mg'_{Sc}). From a qualitative analysis of the valence band edge in the density of states (Figure S3 in the SI) in $MgSc_2S_4(Se_4)$, we speculate that both Mg and Sc bond quite ionically with the anion (S/Se). In contrast, the In−S bonds show significant hybridization in $MgIn_2S_4$ compared to the Sc−S(Se) bonds in $MgSc_2S_4(Se_4)$, stabilizing the p-type Mg'_{In}. These observations could explain the higher concentrations of Mg'_{In} as opposed to Mg'_{Sc}, as indicated by our calculations across all conditions (Table S1).

From this analysis, two criteria to design a ternary spinel ionic conductor with minimal electronic conductivity emerge: (i) Materials with large band gap (curbing the ionization of free carriers) and (ii) materials where both p- and n-type antisites are equally likely to form (leading to spinel inversion and lower free carriers) are preferable.

6.5. Extrinsic Doping. Aliovalent doping of ionic conductors can be used as a strategy to enhance the ionic conductivities while suppressing intrinsic electronic (hole) conductivities. We explored the defect chemistry of extrinsic dopants in the γ-facet of $MgSc_2Se_4$ (Figure 6), comprising tetravalent and pentavalent nonredox cation substitution on Sc as well as halogen doping on Se. Given that the intrinsic E^{eq}_{Fermi} is ∼1.08 eV in anion-poor $MgSc_2Se_4$, doping of most cations is not energetically favored (Figure 6a), with the exception of Ce, Ti, and Zr. Halogen doping on Se appears feasible (E^f < 0.4 eV, Figure 6b), although it may further increase the n-type behavior. In contrast, n-type Ce and Ti have their respective donor transition levels deeper in the band gap (Figure 6a) and may reduce the free-electron concentration in $MgSc_2Se_4$. However, it remains to be experimentally confirmed whether Ti and Ce can be efficiently doped on the Sc site.

7. CONCLUSION

Using first-principles calculations, we have analyzed the role of defect chemistry in influencing the electrical conductivities of three chalcogenide spinels, $MgSc_2Se_4$, $MgSc_2S_4$, and $MgIn_2S_4$, which are potential Mg-ion conductors. We find that intrinsic point defects, such as Mg-metal antisites ($\{Sc/In\}^{\bullet}_{Mg}$, $Mg'_{\{Sc/In\}}$) and Mg-vacancies (Vac''_{Mg}), dramatically affect the free-carrier concentrations of the spinels under consideration. Additionally, controlling the anion content during synthesis is an important factor in determining the defect energetics and the resultant electrical conductivity, with all three spinels exhibiting high n-type conductivity in anion-poor conditions and marginal p-type behavior in anion-rich conditions. Also, fast cooling leads to large concentrations of intrinsic defects being quenched within the structure, which can increase both the free-hole (anion-rich) and free-electron (anion-poor) concentrations in $MgSc_2Se_4$, $MgSc_2S_4$, and $MgIn_2S_4$. Hence, the lowest electronic conductivity is to be expected for samples synthesized under anion excess, and slowly cooled to room temperature. Among the three structures considered, $MgIn_2S_4$ exhibits the lowest free-carrier concentration across various conditions, largely due to inversion within the spinel. Finally, the introduction of aliovalent dopants, such as Ce and Ti on Sc, may mitigate the electronic conductivity observed in $MgSc_2Se_4$. Our work indicates the importance of defects in the field of solid electrolytes, and the framework used here can be applied to other systems as well, which will eventually aid in both the calibration of existing candidates and accelerated material discovery.

■ ASSOCIATED CONTENT

Supporting Information

The Supporting Information is available free of charge on the ACS Publications website at DOI: 10.1021/acs.chemmater.7b02909.

Example of a Freysoldt correction, additional theory on the defect energies, band structures and density of states, ternary phase-diagrams, defect formation energies of native defects, and equilibrium Fermi levels and defect concentrations (PDF)

■ AUTHOR INFORMATION

Corresponding Authors

*E-mail: pcanepa@lbl.gov.
*E-mail: gceder@berkeley.edu.

ORCID

Pieremanuele Canepa: 0000-0002-5168-9253
Gopalakrishnan Sai Gautam: 0000-0002-1303-0976

Present Address

⊥Pieremanuele Canepa: Department of Chemistry, University of Bath, Bath, BA2 7AY, United Kingdom.

Author Contributions

‖P.C. and G.S.G. contributed equally to this work.

Notes

The authors declare no competing financial interest.

■ ACKNOWLEDGMENTS

This work was fully supported as part of the Joint Center for Energy Storage Research (JCESR), an Energy Innovation Hub funded by the U.S. Department of Energy, Office of Science, and Basic Energy Sciences. This study was supported by Subcontract 3F-31144. The authors thank the National Energy Research Scientific Computing Center (NERSC) for providing computing resources. The authors thank Mark D. Asta at UC Berkeley for constructive comments, while P.C. acknowledges Jacques-Arnaud Dâwson for useful discussion.

■ REFERENCES

(1) Hsu, K. F. Cubic $AgPb_mSbTe_{2+m}$: Bulk Thermoelectric Materials with High Figure of Merit. *Science* **2004**, *303*, 818−821.
(2) Snyder, G. J.; Toberer, E. S. Complex thermoelectric materials. *Nat. Mater.* **2008**, *7*, 105−114.
(3) Persson, C.; Zhao, Y.-J.; Lany, S.; Zunger, A. *n*-type doping of $CuInSe_2$ and $CuGaSe_2$. *Phys. Rev. B: Condens. Matter Mater. Phys.* **2005**, *72*, 35211.
(4) Todorov, T. K.; Reuter, K. B.; Mitzi, D. B. High-Efficiency Solar Cell with Earth-Abundant Liquid-Processed Absorber. *Adv. Mater.* **2010**, *22*, E156−E159.
(5) Chen, S.; Walsh, A.; Luo, Y.; Yang, J.-H.; Gong, X. G.; Wei, S.-H. Wurtzite-derived polytypes of kesterite and stannite quaternary chalcogenide semiconductors. *Phys. Rev. B: Condens. Matter Mater. Phys.* **2010**, *82*, 159904.
(6) Sun, R.; Chan, M. K. Y.; Kang, S.; Ceder, G. Intrinsic stoichiometry and oxygen-induced p-type conductivity of pyrite FeS_2. *Phys. Rev. B: Condens. Matter Mater. Phys.* **2011**, *84*, 35212.
(7) Sun, R.; Ceder, G. Feasibility of band gap engineering of pyrite FeS_2. *Phys. Rev. B: Condens. Matter Mater. Phys.* **2011**, *84*, 245211.
(8) Redinger, A.; Berg, D. M.; Dale, P. J.; Siebentritt, S. The Consequences of Kesterite Equilibria for Efficient Solar Cells. *J. Am. Chem. Soc.* **2011**, *133*, 3320−3323.
(9) Baranowski, L. L.; Zawadzki, P.; Christensen, S.; Nordlund, D.; Lany, S.; Tamboli, A. C.; Gedvilas, L.; Ginley, D. S.; Tumas, W.;

DOI: 10.1021/acs.chemmater.7b02909
Chem. Mater. XXXX, XXX, XXX−XXX

Toberer, E. S.; Zakutayev, A. Control of Doping in Cu_2SnS_3 through Defects and Alloying. *Chem. Mater.* **2014**, *26*, 4951−4959.
(10) Kitchaev, D. A.; Ceder, G. Evaluating structure selection in the hydrothermal growth of FeS_2 pyrite and marcasite. *Nat. Commun.* **2016**, *7*, 13799.
(11) Butler, K. T.; McKechnie, S.; Azarhoosh, P.; van Schilfgaarde, M.; Scanlon, D. O.; Walsh, A. Quasi-particle electronic band structure and alignment of the V-VI-VII semiconductors SbSI, SbSBr, and SbSeI for solar cells. *Appl. Phys. Lett.* **2016**, *108*, 112103.
(12) Patrie, M.; Flahaut, J.; Domage, L. Chimie Minerale - Sur Une Nouvelle Serie De Spinelles Soufres Contenant Des Terres Rares Ou Du Scandium. *C. R. Hebd. Acad. Sci.* **1964**, *258*, 2585−2586.
(13) Guittard, M.; Souleau, C.; Farsam, H. Sur Une Nouvelle Serie De Spinelles Selenies Des Terres Rares De layttrium Et Du Scandium. *C. R. Hebd. Acad. Sci.* **1964**, *259*, 2847−2849.
(14) Gamble, F. R.; DiSalvo, F. J.; Klemm, R. A.; Geballe, T. H. Superconductivity in Layered Structure Organometallic Crystals. *Science* **1970**, *168*, 568−570.
(15) Mattheiss, L. F. Band Structures of Transition-Metal-Dichalcogenide Layer Compounds. *Phys. Rev. B* **1973**, *8*, 3719−3740.
(16) Williams, A. J.; McQueen, T. M.; Cava, R. J. The stoichiometry of FeSe. *Solid State Commun.* **2009**, *149*, 1507−1509.
(17) Whittingham, M. S. Chemistry of intercalation compounds: Metal guests in chalcogenide hosts. *Prog. Solid State Chem.* **1978**, *12*, 41−99.
(18) Levi, E.; Gershinsky, G.; Aurbach, D.; Isnard, O.; Ceder, G. New Insight on the Unusually High Ionic Mobility in Chevrel Phases. *Chem. Mater.* **2009**, *21*, 1390−1399.
(19) Kamaya, N.; Homma, K.; Yamakawa, Y.; Hirayama, M.; Kanno, R.; Yonemura, M.; Kamiyama, T.; Kato, Y.; Hama, S.; Kawamoto, K.; Mitsui, A. A lithium superionic conductor. *Nat. Mater.* **2011**, *10*, 682−686.
(20) Ong, S. P.; Mo, Y.; Richards, W. D.; Miara, L.; Lee, H. S.; Ceder, G. Phase stability, electrochemical stability and ionic conductivity of the $Li_{10\pm1}MP_2X_{12}$ (M = Ge, Si, Sn, Al or P, and X = O, S or Se) family of superionic conductors. *Energy Environ. Sci.* **2013**, *6*, 148−156.
(21) Wang, Y.; Richards, W. D.; Ong, S. P.; Miara, L. J.; Kim, J. C.; Mo, Y.; Ceder, G. Design principles for solid-state lithium superionic conductors. *Nat. Mater.* **2015**, *14*, 1026−1031.
(22) Canepa, P.; Bo, S.-H.; Gopalakrishnan, S. G.; Key, B.; Richards, W. D.; Tan, S.; Tian, Y.; Wang, Y.; Li, J.; Ceder, G. High Magnesium Mobility in Ternary Spinel Chalcogenides, accepted in *Nat. Commun.*, **2017**.
(23) Nozik, A. Quantum dot solar cells. *Phys. E* **2002**, *14*, 115−120.
(24) Eisler, H.-J.; Sundar, V. C.; Bawendi, M. G.; Walsh, M.; Smith, H. I.; Klimov, V. Color-selective semiconductor nanocrystal laser. *Appl. Phys. Lett.* **2002**, *80*, 4614.
(25) Talapin, D. V.; Murray, C. B. PbSe Nanocrystal Solids for *n*- and *p*-Channel Thin Film Field-Effect Transistors. *Science* **2005**, *310*, 86−89.
(26) Anikeeva, P. O.; Halpert, J. E.; Bawendi, M. G.; Bulović, V. Quantum Dot Light-Emitting Devices with Electroluminescence Tunable over the Entire Visible Spectrum. *Nano Lett.* **2009**, *9*, 2532−2536.
(27) Meinardi, F.; Colombo, A.; Velizhanin, K. A.; Simonutti, R.; Lorenzon, M.; Beverina, L.; Viswanatha, R.; Klimov, V. I.; Brovelli, S. Large-area luminescent solar concentrators based on 'Stokes-shift-engineered' nanocrystals in a mass-polymerized PMMA matrix. *Nat. Photonics* **2014**, *8*, 392−399.
(28) Jia, S.; Ji, H.; Climent-Pascual, E.; Fuccillo, M. K.; Charles, M. E.; Xiong, J.; Ong, N. P.; Cava, R. J. Low-carrier-concentration crystals of the topological insulator Bi_2Te_2Se. *Phys. Rev. B: Condens. Matter Mater. Phys.* **2011**, *84*, 235206.
(29) Chhowalla, M.; Shin, H. S.; Eda, G.; Li, L.-J.; Loh, K. P.; Zhang, H. The chemistry of two-dimensional layered transition metal dichalcogenide nanosheets. *Nat. Chem.* **2013**, *5*, 263−275.
(30) Behrh, G. K.; Isobe, M.; Massuyeau, F.; Serier-Brault, H.; Gordon, E. E.; Koo, H.-J.; Whangbo, M.-H.; Gautier, R.; Jobic, S. Oxygen-Vacancy-Induced Midgap States Responsible for the Fluorescence and the Long-Lasting Phosphorescence of the Inverse Spinel $Mg(Mg,Sn)O_4$. *Chem. Mater.* **2017**, *29*, 1069−1075.
(31) Griffin, S. M.; Reidulff, M.; Selbach, S. M.; Spaldin, N. A. Defect chemistry as a crystal structure design parameter: Intrinsic Point defects and Ga substitution in $InMnO_3$. *Chem. Mater.* **2017**, *29*, 2425.
(32) Canepa, P.; Gautam, G. S.; Hannah, D. C.; Malik, R.; Liu, M.; Gallagher, K. G.; Persson, K. A.; Ceder, G. Odyssey of Multivalent Cathode Materials: Open Questions and Future Challenges. *Chem. Rev.* **2017**, *117*, 4287−4341.
(33) Freysoldt, C.; Grabowski, B.; Hickel, T.; Neugebauer, J.; Kresse, G.; Janotti, A.; de Walle, C. G. V. First-principles calculations for point defects in solids. *Rev. Mod. Phys.* **2014**, *86*, 253−305.
(34) Zhang, S.; Northrup, J. Chemical potential dependence of defect formation energies in GaAs: Application to Ga self-diffusion. *Phys. Rev. Lett.* **1991**, *67*, 2339−2342.
(35) Laks, D. B.; de Walle, C. G. V.; Neumark, G. F.; Blöchl, P. E.; Pantelides, S. T. Native defects and self-compensation in ZnSe. *Phys. Rev. B: Condens. Matter Mater. Phys.* **1992**, *45*, 10965−10978.
(36) Kwak, K. W.; Vanderbilt, D.; King-Smith, R. D. First-principles study of phosphorus and nitrogen impurities in ZnSe. *Phys. Rev. B: Condens. Matter Mater. Phys.* **1995**, *52*, 11912−11919.
(37) Van de Walle, C. G.; Neugebauer, J. First-principles calculations for defects and impurities: Applications to III-nitrides. *J. Appl. Phys.* **2004**, *95*, 3851−3879.
(38) Freysoldt, C.; Neugebauer, J.; de Walle, C. G. V. Fully *Ab Initio* Finite-Size Corrections for Charged-Defect Supercell Calculations. *Phys. Rev. Lett.* **2009**, *102*, 16402.
(39) Freysoldt, C.; Neugebauer, J.; de Walle, C. G. V. Electrostatic interactions between charged defects in supercells. *Phys. Status Solidi B* **2011**, *248*, 1067−1076.
(40) Broberg, D.; Medasani, B.; Zimmermann, N.; Canning, A.; Haranczyk, M.; Asta, M.; Hautier, G. PyCDT: A Python toolkit for modeling point defects in semiconductors and insulators. *Comput. Phys. Commun.*, submitted for publication, **2016**.
(41) Komsa, H.-P.; Rantala, T. T.; Pasquarello, A. Finite-size supercell correction schemes for charged defect calculations. *Phys. Rev. B: Condens. Matter Mater. Phys.* **2012**, *86*, 45112.
(42) Leslie, M.; Gillan, N. J. The energy and elastic dipole tensor of defects in ionic crystals calculated by the supercell method. *J. Phys. C: Solid State Phys.* **1985**, *18*, 973−982.
(43) Makov, G.; Payne, M. C. Periodic boundary conditions inab initiocalculations. *Phys. Rev. B: Condens. Matter Mater. Phys.* **1995**, *51*, 4014−4022.
(44) Carloni, P.; Blöechl, P. E.; Parrinello, M. Electronic structure of the Cu, Zn superoxide dismutase active site and its interactions with the substrate. *J. Phys. Chem.* **1995**, *99*, 1338−1348.
(45) Schultz, P. A. Charged Local Defects in Extended Systems. *Phys. Rev. Lett.* **2000**, *84*, 1942−1945.
(46) Lany, S.; Zunger, A. Assessment of correction methods for the band-gap problem and for finite-size effects in supercell defect calculations: Case studies for ZnO and GaAs. *Phys. Rev. B: Condens. Matter Mater. Phys.* **2008**, *78*, 235104.
(47) Hohenberg, P.; Kohn, W. Inhomogeneous Electron Gas. *Phys. Rev.* **1964**, *136*, B864−B871.
(48) Kohn, W.; Sham, L. J. Self-Consistent Equations Including Exchange and Correlation Effects. *Phys. Rev.* **1965**, *140*, A1133−A1138.
(49) Perdew, J. P.; Burke, K.; Ernzerhof, M. Generalized Gradient Approximation Made Simple. *Phys. Rev. Lett.* **1996**, *77*, 3865−3868.
(50) Kresse, G.; Hafner, J. *Ab initio* molecular dynamics for liquid metals. *Phys. Rev. B: Condens. Matter Mater. Phys.* **1993**, *47*, 558−561.
(51) Kresse, G.; Furthmüller, J. Efficient iterative schemes forab initiototal-energy calculations using a plane-wave basis set. *Phys. Rev. B: Condens. Matter Mater. Phys.* **1996**, *54*, 11169−11186.
(52) Blöchl, P. E. Projector augmented-wave method. *Phys. Rev. B: Condens. Matter Mater. Phys.* **1994**, *50*, 17953−17979.
(53) Kresse, G.; Joubert, D. From ultrasoft pseudopotentials to the projector augmented-wave method. *Phys. Rev. B: Condens. Matter Mater. Phys.* **1999**, *59*, 1758−1775.

DOI: 10.1021/acs.chemmater.7b02909
Chem. Mater. XXXX, XXX, XXX−XXX

(54) Monkhorst, H. J.; Pack, J. D. Special points for Brillouin-zone integrations. *Phys. Rev. B* **1976**, *13*, 5188−5192.
(55) Ong, S. P.; Richards, W. D.; Jain, A.; Hautier, G.; Kocher, M.; Cholia, S.; Gunter, D.; Chevrier, V. L.; Persson, K. A.; Ceder, G. Python Materials Genomics (pymatgen): A robust, open-source python library for materials analysis. *Comput. Mater. Sci.* **2013**, *68*, 314−319.
(56) Jain, A.; Ong, S. P.; Hautier, G.; Chen, W.; Richards, W. D.; Dacek, S.; Cholia, S.; Gunter, D.; Skinner, D.; Ceder, G.; Persson, K. A. Commentary: The Materials Project: A materials genome approach to accelerating materials innovation. *APL Mater.* **2013**, *1*, 011002.
(57) Heyd, J.; Scuseria, G. E.; Ernzerhof, M. Hybrid functionals based on a screened Coulomb potential. *J. Chem. Phys.* **2003**, *118*, 8207−8215.
(58) Heyd, J.; Scuseria, G. E.; Ernzerhof, M. Erratum: "Hybrid functionals based on a screened Coulomb potential" [J. Chem. Phys. 118, 8207 (2003)]. *J. Chem. Phys.* **2006**, *124*, 219906.
(59) Lejaeghere, K.; et al. Reproducibility in density functional theory calculations of solids. *Science* **2016**, *351*, aad3000−aad3000.
(60) Wang, C. S.; Pickett, W. E. Density-Functional Theory of Excitation Spectra of Semiconductors: Application to Si. *Phys. Rev. Lett.* **1983**, *51*, 597−600.
(61) Chevrier, V. L.; Ong, S. P.; Armiento, R.; Chan, M. K. Y.; Ceder, G. Hybrid density functional calculations of redox potentials and formation energies of transition metal compounds. *Phys. Rev. B: Condens. Matter Mater. Phys.* **2010**, *82*, 75122.
(62) Gastaldi, L.; Lapiccirella, A. Three different methods of determining the cation distribution in spinels: A comparison. *J. Solid State Chem.* **1979**, *30*, 223−229.
(63) Weil, J. A. A review of electron spin spectroscopy and its application to the study of paramagnetic defects in crystalline quartz. *Phys. Chem. Miner.* **1984**, *10*, 149−165.
(64) Livraghi, S.; Paganini, M. C.; Giamello, E.; Selloni, A.; Valentin, C. D.; Pacchioni, G. Origin of Photoactivity of Nitrogen-Doped Titanium Dioxide under Visible Light. *J. Am. Chem. Soc.* **2006**, *128*, 15666−15671.
(65) Wakaki, M.; Shintani, O.; Ogawa, T.; Arai, T. Optical and Electrical Properties of Inverse Spinel Compound $MgIn_2S_4$. *Jpn. J. Appl. Phys.* **1980**, *19*, 255.
(66) Miara, L. J.; Richards, W. D.; Wang, Y. E.; Ceder, G. First-Principles Studies on Cation Dopants and Electrolyte Cathode Interphases for Lithium Garnets. *Chem. Mater.* **2015**, *27*, 4040−4047.
(67) Janek, J.; Zeier, W. G. A solid future for battery development. *Nature Energy* **2016**, *1*, 16141.
(68) Kato, Y.; Hori, S.; Saito, T.; Suzuki, K.; Hirayama, M.; Mitsui, A.; Yonemura, M.; Iba, H.; Kanno, R. High-power all-solid-state batteries using sulfide superionic conductors. *Nature Energy* **2016**, *1*, 16030.
(69) Pauling, L. The theoretical prediction of the physical properties of many-electron atoms and ions. Mole refraction, diamagnetic susceptibility, and extension in space. *Proc. R. Soc. London, Ser. A* **1927**, *114*, 181−211.
(70) Burdett, J. K.; Price, G. D.; Price, S. L. Factors influencing solid-state structure—an analysis using pseudopotential radii structural maps. *Phys. Rev. B: Condens. Matter Mater. Phys.* **1981**, *24*, 2903−2912.
(71) Burdett, J. K.; Price, G. D.; Price, S. L. Role of the crystal-field theory in determining the structures of spinels. *J. Am. Chem. Soc.* **1982**, *104*, 92−95.
(72) Sickafus, K. E.; Wills, J. M.; Grimes, N. W. Structure of Spinel. *J. Am. Ceram. Soc.* **1999**, *82*, 3279−3292.
(73) Zhang, X.; Zunger, A. Diagrammatic Separation of Different Crystal Structures of A_2BX_4 Compounds Without Energy Minimization: A Pseudopotential Orbital Radii Approach. *Adv. Funct. Mater.* **2010**, *20*, 1944−1952.
(74) Lucero, M. J.; Aguilera, I.; Diaconu, C. V.; Palacios, P.; Wahnón, P.; Scuseria, G. E. Screened hybrid and self-consistent GW calculations of cadmium/magnesium indium sulfide materials. *Phys. Rev. B: Condens. Matter Mater. Phys.* **2011**, *83*, 205128.
(75) Stevanović, V.; d'Avezac, M.; Zunger, A. Simple Point-Ion Electrostatic Model Explains the Cation Distribution in Spinel Oxides. *Phys. Rev. Lett.* **2010**, *105*, 075501.
(76) Paudel, T. R.; Zakutayev, A.; Lany, S.; d'Avezac, M.; Zunger, A. Doping Rules and Doping Prototypes in A_2BO_4 Spinel Oxides. *Adv. Funct. Mater.* **2011**, *21*, 4493−4501.
(77) Stevanović, V.; d'Avezac, M.; Zunger, A. Universal Electrostatic Origin of Cation Ordering in A_2BO_4 Spinel Oxides. *J. Am. Chem. Soc.* **2011**, *133*, 11649−11654.
(78) Das, D.; Ghosh, S. First-principles investigations into the thermodynamics of cation disorder and its impact on electronic structure and magnetic properties of spinel Co $(Cr_{1-x}Mn_x)_2O_4$. *J. Phys.: Condens. Matter* **2017**, *29*, 055805.
(79) Shannon, R. D. Revised effective ionic radii and systematic studies of interatomic distances in halides and chalcogenides. *Acta Crystallogr., Sect. A: Cryst. Phys., Diffr., Theor. Gen. Crystallogr.* **1976**, *32*, 751−767.
(80) Sai Gautam, G.; Canepa, P.; Urban, A.; Bo, S.-H.; Ceder, G. Influence of Inversion on Mg Mobility and Electrochemistry in Spinels. *Chem. Mater.* **2017**, *29*, 7918−7930.

DOI: 10.1021/acs.chemmater.7b02909
Chem. Mater. XXXX, XXX, XXX−XXX